



27 eastern Arkansas, the third most irrigated state in the USA. Our results show that the presence
28 of OFRs in the watershed decreased annual flow on average between 14 and 24%, and the
29 mean reduction in peak flow varied between 43 and 60%. In addition, the cumulative impact
30 of the OFRs was not equally distributed across the watershed, and it varied according to the
31 OFR spatial distribution, and their storage capacity. The results of this study and the proposed
32 framework can support water agencies with information on the cumulative impact of OFRs,
33 aiming to support surface water resources management. This is relevant as the number of
34 OFRs is expected to increase globally as an adaptation to climate change under severe
35 drought conditions.

36

37 1 Introduction

38 Inland water bodies (e.g., lakes and reservoirs) comprise a small fraction of Earth's surface;
39 however, they are responsible for storing the vast majority of the accessible fresh water
40 resources available on Earth. In addition, these water bodies are pivotal components of surface
41 hydrology, having key roles in ecosystem functioning and wildlife habitats (Khazaei et al., 2022;
42 Verpoorter et al., 2014). In particular, on-farm reservoirs (OFRs) are essential to meet global
43 irrigation needs (Döll et al., 2009; Downing, 2010; Van Den Hoek et al., 2019). Farmers use OFRs
44 to store water from precipitation and runoff during the rainy season to irrigate their crops
45 during the dry season (Habets et al., 2018; Perin et al., 2021; Vanthof & Kelly, 2019; Yaeger et al.,
46 2017; Yaeger et al., 2018). The number of OFRs is expected to rise worldwide in the coming
47 decades, and estimates show that there are more than 2.1 million OFRs in the US alone
48 (Downing, 2010; Renwick et al., 2005). OFRs are often built to manage surface water resources
49 more efficiently, and to help mitigate the impact of extreme droughts, which are projected to
50 increase due to climate change (Habets et al., 2018; Van Der Zaag & Gupta, 2008). Although
51 OFRs are small water bodies (< 50 ha), they can have cumulative impacts on the local and
52 remote hydrology in the watersheds where they occur (e.g., decreasing flow and peak flow)



53 (Habets et al., 2018), and their impact may contribute to worsening the surface water stress
54 already intensified by climate change and population growth (Vörösmarty et al., 2010). Most
55 studies have focused on the cumulative impact of major large reservoirs on downstream flow
56 alteration (Chalise et al., 2021; Mukhopadhyay et al., 2021), but limited analysis has been
57 performed on the impact of OFRs on downstream flow availability.

58 To quantify the impact of OFRs on surface hydrology, it is necessary to understand the
59 spatial and temporal variability of OFRs, as well as how the impacts are related to the OFR
60 networks, as the impacts of OFRs are not the sum of the individual OFR impacts, but rather
61 the sum and their interaction effects (Canter & Kamath, 1995; Habets et al., 2018). By gathering
62 information from several studies conducted in different countries (e.g., USA, France, Brazil),
63 Habets et al., (2018) did a thorough assessment of the OFRs' impact on surface hydrology, and
64 the different types of models and ways to represent the OFRs on the watershed. The authors
65 concluded that the modeled OFRs impacts have a wide range, and that most of the studies
66 reported a mean annual reduction in flow, which ranged between 0.2 and 36%. In addition, the
67 variability of the impact as identified in these previous studies was higher when assessing low
68 flows during multiple years, with reductions between 0.3 and 60%. In general, the estimated
69 mean annual reduction in flow was $13.4\% \pm 8.0\%$, and the mean decrease in peak flow was up
70 to 45% (Habets et al., 2018).

71 The approaches used to quantify the cumulative impact of OFRs can be divided into
72 two classes: data-driven methods, and process based hydrological modeling. The data-driven
73 approaches include three main methods. The first method relies on assessing measured
74 inflows and outflows of selected OFRs aiming to quantify their hydrological functioning with
75 the assumption that the cumulative impacts are the sum of individual impacts (Culler et al.,
76 1961; Dubreuil and Girard, 1973; Kennon, 1966). A variation of the cumulative impact assessment
77 approach has been recently suggested by Hwang et al., (2021) by comparing the naturalized
78 flows and the controlled flows for assessing the impact of large reservoir systems. The second
79 method is based on statistical analysis of the observed discharge time series of a watershed as



80 the number of OFRs increased (Galéa et al., 2005; Schreider et al., 2002). This approach is limited
81 when discriminating the specific impact of OFRs from those of land use and land cover
82 change, and when explicitly representing the OFRs in the models, given that OFRs tend to be
83 aggregated within the entire basin (i.e., OFRs surface area and/or storage are summed and
84 modeled as a unique water impoundment). The third method relies on conducting a paired-
85 catchment experiment by comparing the flows from two adjacent and similar catchments,
86 one with OFRs and the other without OFRs (Thompson, 2012). This technique requires the
87 catchment properties (e.g., soils, topology, lithology, land cover) to be spatially homogeneous,
88 which is practically nonexistent at a large scale, hence limiting this method's applications.

89 The second class of methods relate to hydrological modeling, and it is the most widely
90 used approach for assessing the OFRs' impacts. A variety of models have been proposed by
91 coupling the OFRs' water balance with a quantitative approach to estimate the OFRs' water
92 volume change (Fowler et al., 2015; Habets et al., 2014; Jalowska & Yuan, 2019; Yongbo et al.,
93 2014; Ni & Parajuli, 2018; Perrin, 2012; Zhang et al., 2012). In general, the models have three main
94 components: the OFR water balance, the quantitative approach to quantify the OFR inflows,
95 and the spatial representation of the OFRs network. These different model components result
96 in different limitations and assumptions—a complete assessment of these three components
97 and how they impact the hydrological simulations is provided in a recent review (Habets et al.,
98 2018). Therefore, when selecting a specific model to assess the impacts of the OFRs, it is
99 important to account for the model's suitability for the target issue to be addressed, as well as
100 the model limitations and assumptions. The selected model should also have capability to
101 incorporate/assimilate varying land-surface conditions (e.g., soil moisture) and time-varying
102 OFR storages which could be obtained either from local monitoring or through remote
103 sensing.

104 Most studies have used remotely-sensed products such as soil moisture (e.g., SMAP;
105 (Entekhabi et al., 2010), groundwater (e.g., GRACE; (Tapley et al., 2004) and land cover
106 conditions (e.g., MODIS; (Justice et al., 1998)) for assimilating current conditions into



107 hydrological models. Given that OFRs tend to occur in high numbers (e.g., hundreds), multiple
108 studies leveraged the latest developments and availability of satellite imagery to monitor the
109 occurrence and dynamics of OFRs (Jones et al., 2017; Ogilvie et al., 2018, 2020; Perin et al., 2022;
110 Perin et al., 2021a, 2021b; Van Den Hoek et al., 2019; Vanthof & Kelly, 2019), which could provide
111 useful information on local storage conditions for predicting downstream streamflow. Further,
112 these studies allowed quantifying the number of OFRs, and their spatial and temporal
113 variability in surface water area and storage in the watershed where they occur, providing
114 relevant information when modeling the cumulative impact of OFRs. Despite the
115 complementary information provided by satellite imagery, there are only a few studies that
116 incorporated remote sensing-derived information (e.g., soil moisture derived from SMAP,
117 groundwater based on GRACE) with hydrological modeling (Ni and Parajuli, 2018; Yongbo et
118 al., 2014; Zhang et al., 2012), and these studies are limited to mapping the OFRs occurrence, or
119 to snapshots of the OFRs conditions (e.g., surface area). To the best of our knowledge, there is
120 no study that combines the spatial and temporal variability of the OFRs—derived using multi-
121 year satellite imagery time series analyses—with a process-based hydrological model.

122 Therefore, to gain novel understanding of the cumulative impact of OFRs on surface
123 hydrology, in this study, we propose a new approach that systematically integrates the
124 dynamically varying conditions of OFRs based on satellite imagery time series (Perin et al.,
125 2022) using a top-down data driven approach within the latest SWAT+ model. The Soil and
126 Water Assessment Tool (SWAT) (Arnold et al., 2012) has been widely used to model the impacts
127 of the OFRs (Jalowska and Yuan, 2019; Kim and Parajuli, 2014; Ni et al., 2020; Ni and Parajuli,
128 2018; Perrin, 2012; Rabelo et al., 2021; Yongbo et al., 2014; Zhang et al., 2012), in part given by a
129 comprehensive collection of model documentation and guidelines available online
130 (<https://swat.tamu.edu/>). Our objectives are to (1) assess the spatial and temporal variability of
131 the cumulative impact of OFRs at the watershed and subwatersheds levels, and (2) to quantify
132 the intra- and-inter annual impacts of the OFRs on flow and peak flow at the channel scale. By
133 integrating the SWAT+ model with a novel remote sensing assimilation algorithm to account

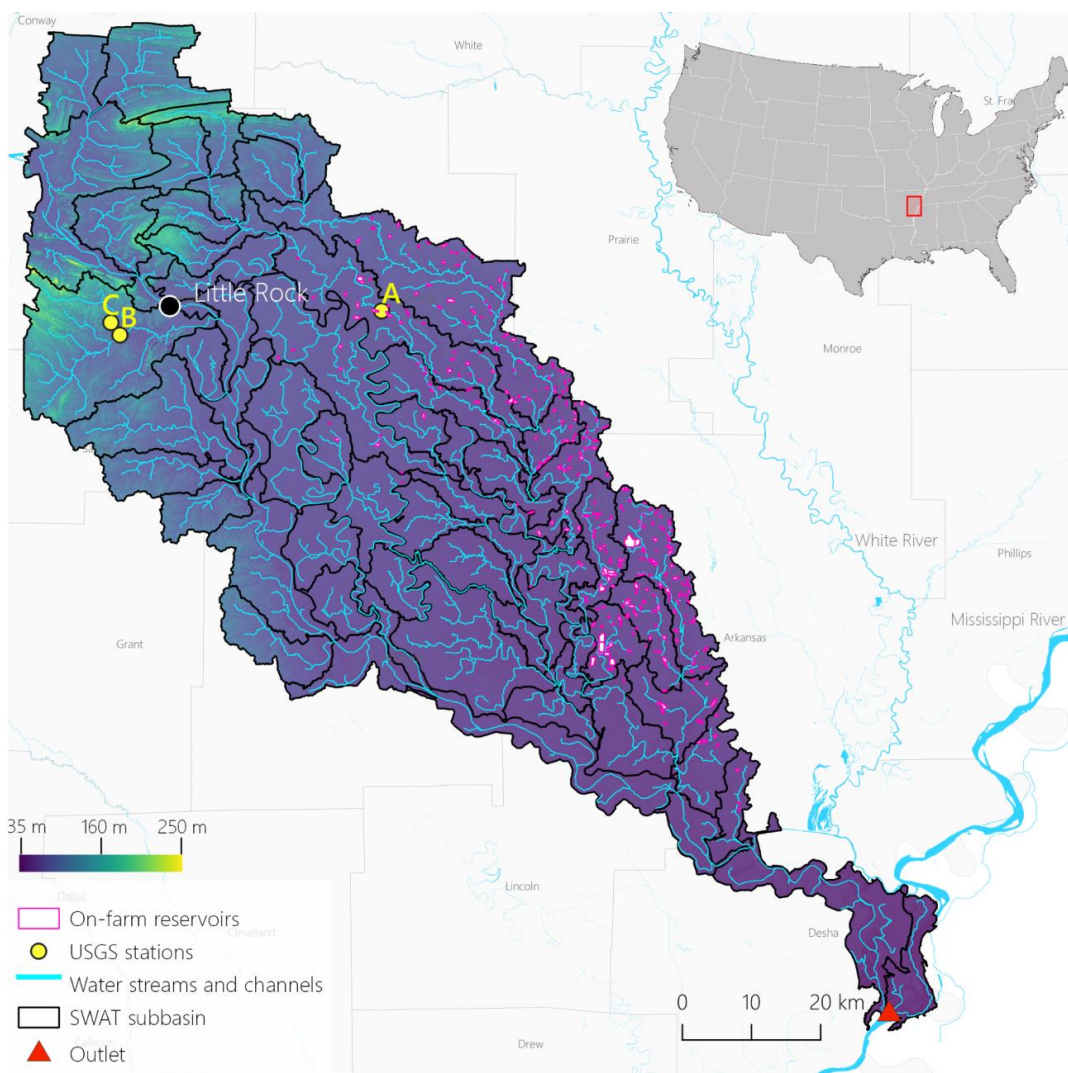


134 for the OFRs spatial variability—which is lacking in most of studies assessing the OFRs
135 impacts—and leveraging a digitally-mapped OFRs dataset (Yaeger et al., 2017), we are
136 providing a new approach that can be replicated in watersheds across the world, and used to
137 support water agencies with information to improve surface water resources management.

138 2 Methods

139 2.1 Study region

140 The study region is located in eastern Arkansas, USA, the third most-irrigated state in the USA
141 (ERS-USDA, 2017). The area has a humid subtropical climate with a 30-year annual average
142 precipitation of ~1300 mm/year (PRISM Climate Group, 2022). The precipitation is distributed
143 mostly between March and May, receiving an average of ~400 mm during these months (Perin
144 et al., 2021b). The region has experienced a steady increase in irrigated agriculture, with
145 commonly irrigated crops including corn, rice, and soybeans (NASS-USDA, 2017). A recent
146 study (Yaeger et al., 2017) digitally mapped 330 OFRs located in the study region (Fig. 1) using
147 the high-resolution (1-m) National Agricultural Imagery Program archive in combination with
148 2015 sub-meter spatial resolution Google Earth satellite imagery. Most of the OFRs (95%) have
149 surface area < 50 ha, and they are concentrated in the eastern portion of the study region (Fig.
150 1).



151
152 **Figure 1**–Study region located in eastern Arkansas, USA, the subwatersheds and surface water
153 streams and channels delineated with SWAT+, the model outlet, the United States Geological
154 Survey (USGS) stations (United States Geological Survey Water Data for the Nation, 2022) used
155 for flow calibration and validation, the digitized OFRs (Yaeger et al., 2017), and the Digital
156 Elevation Model (DEM) used in the modeling (Farr et al., 2007).



157 2.2 SWAT+ model setup

158 2.2.1 The Soil Water Assessment Tool to model the impacts of OFRs on surface hydrology

159 The SWAT model is a time-continuous semi-distributed hydrological model widely used across
160 the globe—more than 5,000 peer reviewed publications since its launch in the early 1980s
161 (Publications | Soil & Water Assessment Tool (SWAT), 2022). The large number of SWAT
162 applications globally revealed the model development needs and its limitations. To address
163 the present and future challenges when modeling with SWAT, the model source code has
164 undergone major modifications, and a completely revised version of the model was proposed
165 in SWAT+ (Bieger et al., 2017). SWAT+ uses the same equations as SWAT to simulate the
166 hydrological processes; however, it offers more flexibility to users when configuring the model
167 (e.g., when defining management schedules, routing constituents, and connecting managed
168 flow systems to the natural stream network) (Bieger et al., 2017).

169 The SWAT+ is under constant improvements (Chawanda et al., 2020; Molina-Navarro et
170 al., 2018), and a new module (Molina-Navarro et al., 2018) was recently developed to allow the
171 optimal integration of a water body and its drainage area within the simulated hydrological
172 processes. In previous versions of the model, when delineating the watershed area draining
173 into a water body, the users were required to place an outlet in a certain point of the water
174 stream's network, and the areas in-between the rivers' subwatersheds flowing into the water
175 body were therefore excluded—if these areas are disregarded, important hydrological
176 processes (e.g., evaporation, overland and/or groundwater flow) flowing into the water body
177 are not accounted for (Molina-Navarro et al., 2018). This former approach can lead to
178 inaccuracies when delineating the watershed areas, especially when the results are used as
179 input to an OFR model component. The newest versions of SWAT+ consider the OFRs' outline
180 (i.e., shape and surface area) when delineating the watersheds; hence, accounting for the
181 entire drainage area flowing into the waterbody (Mollina-Navarro et al., 2018). In addition, the
182 latest versions allow adding more than one OFR per subwatershed by associating the OFR



183 with channels—components of the watersheds, and finer divisions and extensions of water
184 stream reaches—enabling the modeling analyses at the channel scale. When simulating the
185 impact of the OFRs at the channel scale, there is a higher level of detail of where and when the
186 OFRs are contributing to changes in surface hydrology, unlike the previous versions of the
187 model, which allowed adding only a single OFR per subwatershed placed at the subwatershed
188 outlet as a point (Arnold et al., 2012), and therefore, the analyses were conducted at the
189 subwatershed scale.

190 We modeled the impact of OFRs on surface hydrology using the QSWAT+ (v.2.1.9)
191 SWAT+ model interface together with SWAT+ Editor (v.2.1.0) to set up the model, to input the
192 required datasets (e.g., DEM, land use and land cover layer, interpolated meteorological
193 climate information), and to run the different modeling scenarios.

194 The modeled watershed (710,700 ha, Fig. 1) included 68 subwatersheds and a total of
195 642 Hydrological Response Units (HRUs)—HRUs are unique portions of the subwatersheds
196 that have unique land use and management, and soil attributes. We set up daily simulations
197 for 30 years (1990–2020), including five years of model warm up to establish the initial soil water
198 conditions and hydrological processes. The watershed was delineated using the Shuttle Radar
199 Topography Mission DEM (30 m) (Farr et al., 2007). In addition, we set the channel length
200 threshold to 6 km², and the stream length threshold to 60 km². We placed an outlet in the
201 southern part of the study region—where the lowest part of the watershed is located (Fig. 1).
202 We created the HRUs using the dominant option—this option selects the largest HRU within
203 the subwatershed as the general HRU—within QSWAT+ interface, and used the National Land
204 Cover Database (30 m) (Homer et al., 2020), and Gridded Soil Survey Geographic Database
205 (gSSURGO) (Soil Survey Staff, USDA-NRCS, 2021) (100 m) as inputs to the model. The gSSURGO
206 layers were processed according to their guidelines when using them on QSWAT+ (George,
207 2020). For climate data, we extracted the centroid coordinates of each subwatershed (Muche
208 et al., 2020), and used these centroids to download 30 years of daily precipitation, minimum
209 and maximum temperature, surface downward shortwave radiation, wind velocity, and



210 relative humidity from the Gridded Surface Meteorological Datasets (Abatzoglou, 2013),
211 available in Google Earth Engine (Gorelick et al., 2017). The time series of each subwatershed
212 centroid was added into the SWAT+ Editor as independent weather stations.

213 2.2.2 Model calibration and validation procedures

214 We used monthly measured flow from three USGS stations (Fig. 1 and Table 1) to calibrate and
215 validate the model flow simulations. The USGS flow time series length varied between 14 and
216 25 years, and we used 60% of the timeseries for calibration and 40% for validation for each
217 USGS station (Table 1). We assessed the performance of the model by calculating the
218 Coefficient of determination (r^2), Percent bias (PBIAS, %, Eq. 1) (Yapo et al., 1996), and the Nash–
219 Sutcliffe model efficiency coefficient (NSE, Eq. 2) (Nash and Sutcliffe, 1970). PBIAS is the relative
220 mean difference between the simulated and the measured flow values, and it reflects the
221 ability of the model to simulate monthly flows. The optimal PBIAS is zero, and low-magnitude
222 values indicate better model performance. Positive PBIAS indicates overestimation bias,
223 whereas negative values denote underestimation bias. The NSE expresses how well the model
224 simulates flows, and it ranges from a negative value to one, with one indicating a perfect fit
225 between the simulated and measured flow values. In general, the model simulations of
226 monthly flow are considered satisfactory when r^2 ranges from 0.60 to 0.75, PBIAS ranges from
227 $\pm 10\%$ to $\pm 15\%$, and NSE ranges from 0.50 to 0.70 (Moriasi et al., 2015).

228 **Table 1**—USGS stations, drainage areas, and the periods used for flow calibration and validation.

USGS station	Station id	Drainage Area (ha)	Period (years)	
			Calibration	Validation
07264000	(A)	53,600	1995–2010	2010–2020
07263555	(B)	25,400	2007–2014	2014–2020
07263580	(C)	5,300	1997–2011	2011–2020

229



230
$$PBIAS = \frac{\sum_{i=1}^n (Y_i - X_i)}{\sum_{i=1}^n X_i}$$

231 (1)

232
$$NSE = 1 - \frac{\sum_{i=1}^n (X_i - Y_i)^2}{\sum_{i=1}^n (X_i - \bar{X})^2}$$
 (2)

233 Where X_i is the measured flow and Y_i is the simulated flow.

234 We conducted a sensitivity analysis using the SWAT+ ToolBox (v.0.7.6) (SWAT+ Toolbox,
 235 2022) to reveal the most sensitive parameters when simulating flow—a total of 10 parameters
 236 (Table S 1) were tested based on previous studies that used SWAT/SWAT+ to model the impact
 237 of water impoundments on surface hydrology (Jalowska & Yuan, 2019; Yongbo et al., 2014; Ni et
 238 al., 2020; Ni & Parajuli, 2018; Perrin, 2012; Rabelo et al., 2021; Zhang et al., 2012). Following the
 239 sensitivity analysis, we selected the five most sensitive parameters (Table 2), and proceeded
 240 with a manual calibration using the SWAT+ Toolbox. We aimed to improve the model's
 241 monthly flow predictions by testing the parameters one at a time and changing their values
 242 between -20% to 20% with 5% increments based on their range values. The final calibrated
 243 parameters and their fitted values are shown in Table 2.

244 **Table 2**—Monthly flow calibration parameters.

Parameter	Description	Range	Value
CN2	SCS runoff curve number	35–95	0.20*
SOL_AWC	Available water capacity (mm/mm)	0.01–1	-0.20*
ESCO	Soil evaporation compensation coefficient	0.01–1	0.50
PERCO	Percolation coefficient (fraction)	0–1	0.60
CANMX	Maximum canopy storage (mm)	0–100	75

245 *Denotes relative percentage change.

246 **2.3 OFRs representation in SWAT+**

247 Multiple OFRs can be added to the same subwatershed by associating them with channels
 248 (Dile et al., 2022). The OFRs need to have at least one outlet channel, and they may have none
 249 or multiple inlets. Therefore, most OFR-related processes within the model involve



250 determining what channels form inflowing and outflowing channels for each OFR. Ideally,
251 each OFR would interact with a channel, and therefore, have a channel entering, leaving, or
252 within the OFR. Nonetheless, it is common to have OFRs that do not intersect with any channel
253 (Dile et al., 2022)—this is the case for 93% of the OFRs in our study region. The OFRs from our
254 study region are not dammed along the streams, but rather they are engineered water
255 impoundments that are indirectly connected to the main streams via pipes and pumps
256 (Yaeger et al., 2017). A possible solution would be modifying the OFRs' shapes by dragging
257 them to the closest channel (Dile et al., 2022). However, this would require extensive
258 modifications of the OFRs' shapes. In addition, when an OFR is added to a channel, this channel
259 is split into two channels, and the model needs to account for the two newly created channels
260 during the water routing calculations. For this reason, adding multiple OFRs to the same
261 channel, or adding multiple OFRs closely located to the same channel, can be a cumbersome
262 process that leads to numerous routing errors.

263 To overcome these challenges, we aggregated the OFRs' surface area, and added
264 aggregated OFRs to the model. This adaptation involved two steps. First, for each of the 330
265 OFRs, we searched for the closest channel by calculating the distance between the OFRs'
266 centroid and the multiple channels within each subwatershed. Then, we aggregated all the
267 OFRs that were associated with each channel by summing up their surface area, and adding
268 a polygon of the aggregated area to represent the aggregated OFR. This approach resulted in
269 69 aggregated OFRs that were added to 67 different channels located in 16 subwatersheds.
270 The surface area of the aggregated OFRs varied between 3.05 ha and 165.67 ha, and the
271 number of OFRs in each aggregated OFR varied between 2 and 12. To avoid confusion, for the
272 rest of the manuscript, we refer to OFRs as the aggregated OFRs, and not the individual OFRs
273 shown in Fig. 1. For each of the aggregated OFR, the water volume was calculated using SWAT+
274 default rule, which is a simple multiplication of the OFR surface area by a factor of 10, similar
275 to other studies based on SWAT+ (Ni and Parajuli, 2018; Zhang et al., 2012). In addition, given that
276 we did not have access to the OFRs release rates, we used the model default release rule, which



277 sets the OFRs to release water when the spillway volume is reached—80% of the OFRs capacity
278 (Bieger et al., 2017).

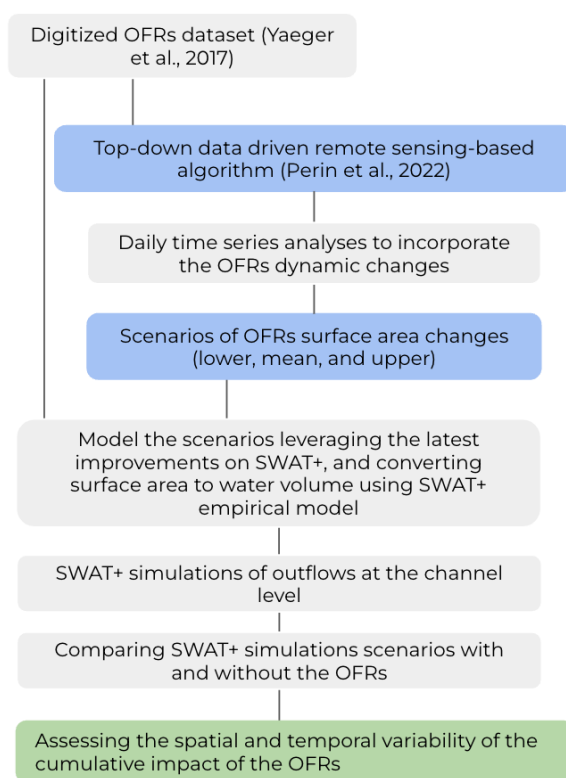
279 2.4 Scenario Analysis

280 Given our representation of the OFRs in SWAT+, we assessed the impact of the OFRs on surface
281 hydrology at the channel scale. To do so, we established the model baseline scenario without
282 the presence of the OFRs on the watershed. In addition, we divided the channels into four
283 classes (i.e., low and high flow classes) according to their mean baseline flow. The different class
284 intervals were calculated using the mean flow quartiles accounting for all channels, which
285 resulted in the following baseline flow classes: (1) 0.001–0.25 m³/s, (2) 0.25–0.50 m³/s, (3) 0.50–2.11
286 m³/s, and (4) 2.11–17.50 m³/s.

287 To account for the OFRs variation in surface area (i.e., change in storage capacity), we
288 propose a novel approach that leverages a top-down data-driven model based on satellite
289 imagery (Fig. 2). We used this model to create three modeling scenarios using daily OFRs
290 surface area time series—these scenarios were based on the methodology proposed by Perin
291 et al., (2022). The authors used a multi-sensor satellite imagery approach with the Kalman filter
292 (Kalman, 1960) to derive daily OFRs' surface area change between 2017 and 2020. The proposed
293 algorithm accounts for the uncertainties in both the sensor's observations and the resulting
294 surface areas. By improving the OFRs surface area observations cadence, the algorithm allows
295 further understanding of the OFRs surface area intra- and inter-annual changes, which are key
296 pieces of information that can be used to better assess and manage the water stored by the
297 OFRs (Perin et al., 2022). The daily surface area time series—derived by combining PlanetScope,
298 RapidEye, and Sentinel-2 satellite imagery (Perin et al., 2022)—of each OFR was used to
299 simulate three scenarios (i.e., lower, mean, and upper) representing the OFRs' capacity in terms
300 of surface area. The mean scenario represents the regular condition of the OFRs, and it is the
301 mean of the daily surface area time series derived from the Kalman filter. The lower and upper
302 scenarios represent the lowest and highest capacities of the OFRs, and they are based on the



303 surface area 95% confidence interval limits, calculated using the daily time series. For each
304 scenario, the OFRs were simulated at full capacity (i.e., maximum storage at the lower, mean
305 and upper scenarios), and this capacity was kept constant during the simulation period (Ni et
306 al., 2020; Ni and Parajuli, 2018; Perrin, 2012). To assess the impact of the OFRs on surface
307 hydrology, we compared the baseline flow with the flow simulated by each surface area
308 scenario—i.e., comparing the flow changes with and without OFRs, a common approach used
309 by previous studies (Habets et al., 2018).



310

311 **Figure 2**—A new approach to integrate a top-down data driven remote sensing-based
312 algorithm, that assesses the OFRs dynamic conditions (Perin et al., 2022), with the latest SWAT+
313 model developments.

314 We estimated the impact of the OFRs on surface hydrology by calculating the percent
315 change (Eq. 3) of monthly flow between the baseline and the three surface area scenarios



316 including all OFRs. The annual impact on flow was calculated by averaging the mean percent
317 change along the months. We also calculated the distribution of the percent change for each
318 baseline flow class. The distribution was assessed using 2-D Kernel Density estimation (KDE)
319 plots. Different from discrete bins (e.g., histograms), the KDE plots show a continuous density
320 estimate of the observations using a Gaussian kernel. In addition, we assessed the percent
321 changes in peak flow. For the purposes of this analysis, peak flow is defined as equal or higher
322 than the 99th flow percentile calculated using the entire flow time series (Eq. 3).

$$323 \quad \text{Percent change (\%)} = \left(\frac{Y_i - X_i}{X_i} \right) * 100 \quad (3)$$

324 Where X_i is the baseline flow and Y_i is the simulated flow of each surface area scenario.

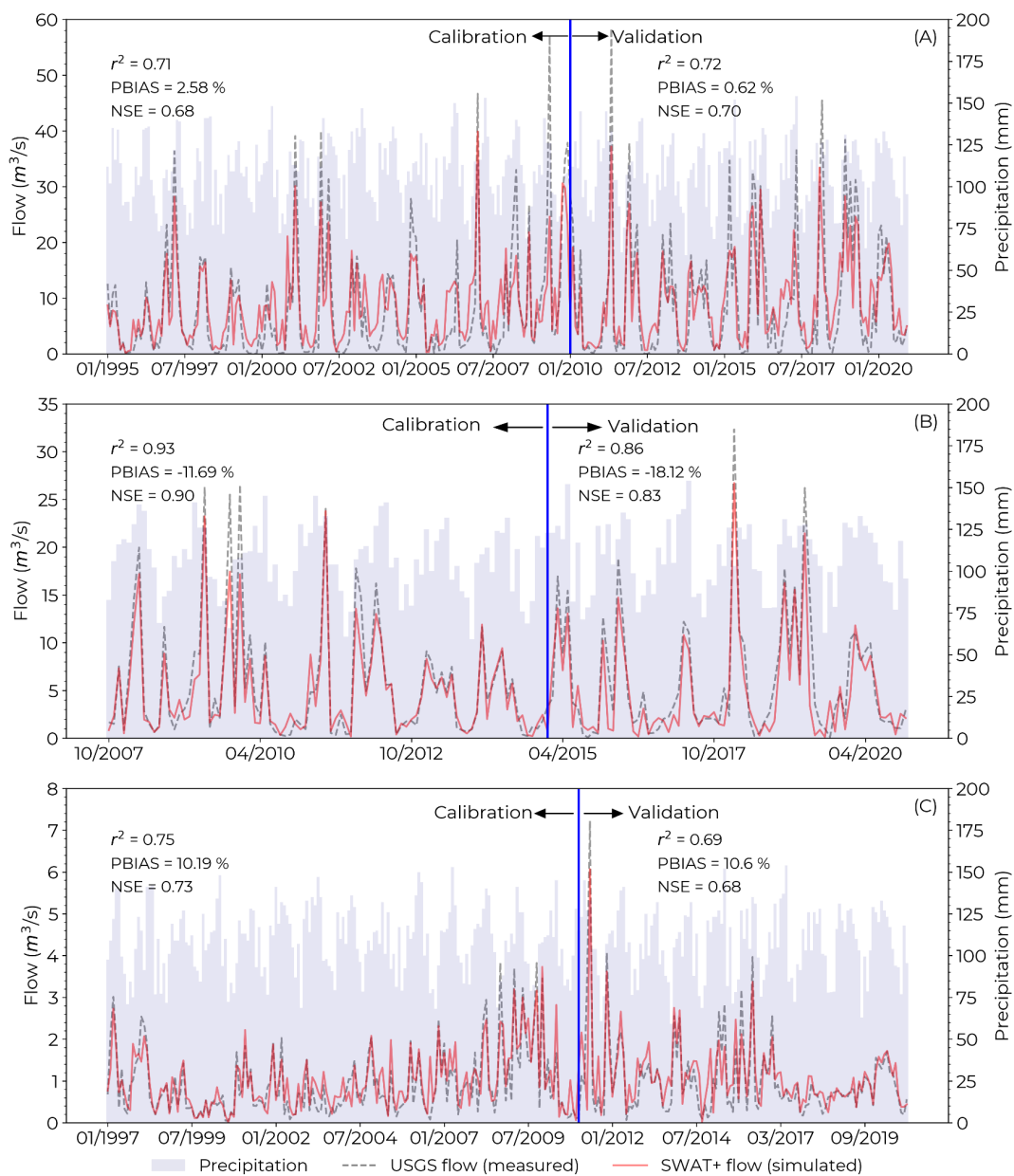
325 3 Results

326 3.1 Model calibration and validation

327 The model calibration and validation were done using the three USGS stations presented in
328 Fig. 1 and Table 1, and accounting for all OFRs in study region. When comparing the monthly
329 simulated flow with the measured flow for the calibration period, there was a good agreement
330 ($0.71 \leq r^2 \leq 0.93$), and a satisfactory model efficiency ($0.68 \leq \text{NSE} \leq 0.90$) for all three stations
331 (Fig. 3). In addition, the PBIAS magnitude was $< 3\%$ for station A, and $< 12\%$ for stations B and C.
332 Meanwhile, the validation period had r^2 ranging between 0.69 and 0.86, and the NSE between
333 0.68 and 0.83, with PBIAS magnitude $< 10\%$ for stations A and B, and 18.12% for station C. In
334 general, for stations A and C, the model overestimated flow values (i.e., positive PBIAS) mostly
335 during flow events $< 3 \text{ m}^3/\text{s}$, and the model underestimated flow (i.e., negative PBIAS) for
336 station B during flows $> 20 \text{ m}^3/\text{s}$ (Fig. 3). These findings are consistent with a previous study
337 conducted in western Mississippi near our study region (Ni and Parajuli, 2018). Even though
338 during the validation period the station B had PBIAS magnitude higher than 15%, the r^2 and
339 NSE values from the calibration and validation periods indicate satisfactory modeling
340 performance when simulating monthly flow (Moriasi et al., 2015). Given that none of the OFRs



341 were directly connected with the streams where the stations were located (Fig. 1), and there
342 were no OFRs nearby stations B and C, the calibration and validation metrics with and without
343 the OFRs were very similar, with differences smaller than 1%.



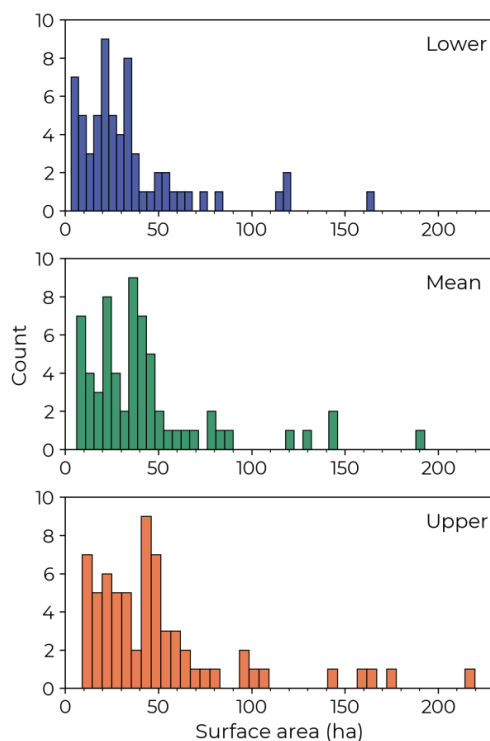
344



345 **Figure 3**—Flow calibration and validation time series for the three USGS stations A (07264000),
346 B (07263555) and C (07263580). See Fig. 1 and Table 1 for more information about the USGS
347 stations. The precipitation time series represents the monthly accumulated precipitation at
348 the watershed scale (i.e., for the entire study region).

349 3.2 Percent change in flow

350 We assessed the impact of the OFRs on flow by comparing the baseline flow (i.e., without the
351 OFRs) with the three surface area scenarios generated from the Kalman filter approach—
352 lower, mean, and upper (see section 2.4, and Fig. 2). The total surface area (i.e., summing all
353 OFRs surface area) was 2.176 ha for the lower, 2.766 ha for the mean, and 3.370 ha for the upper,
354 and the three scenarios had a similar OFRs surface area distribution (Fig. 4). In addition, most
355 of the OFRs had surface areas < 50 ha—78%, 71%, and 62% of the OFRs for the lower, mean, and
356 upper scenarios.



357



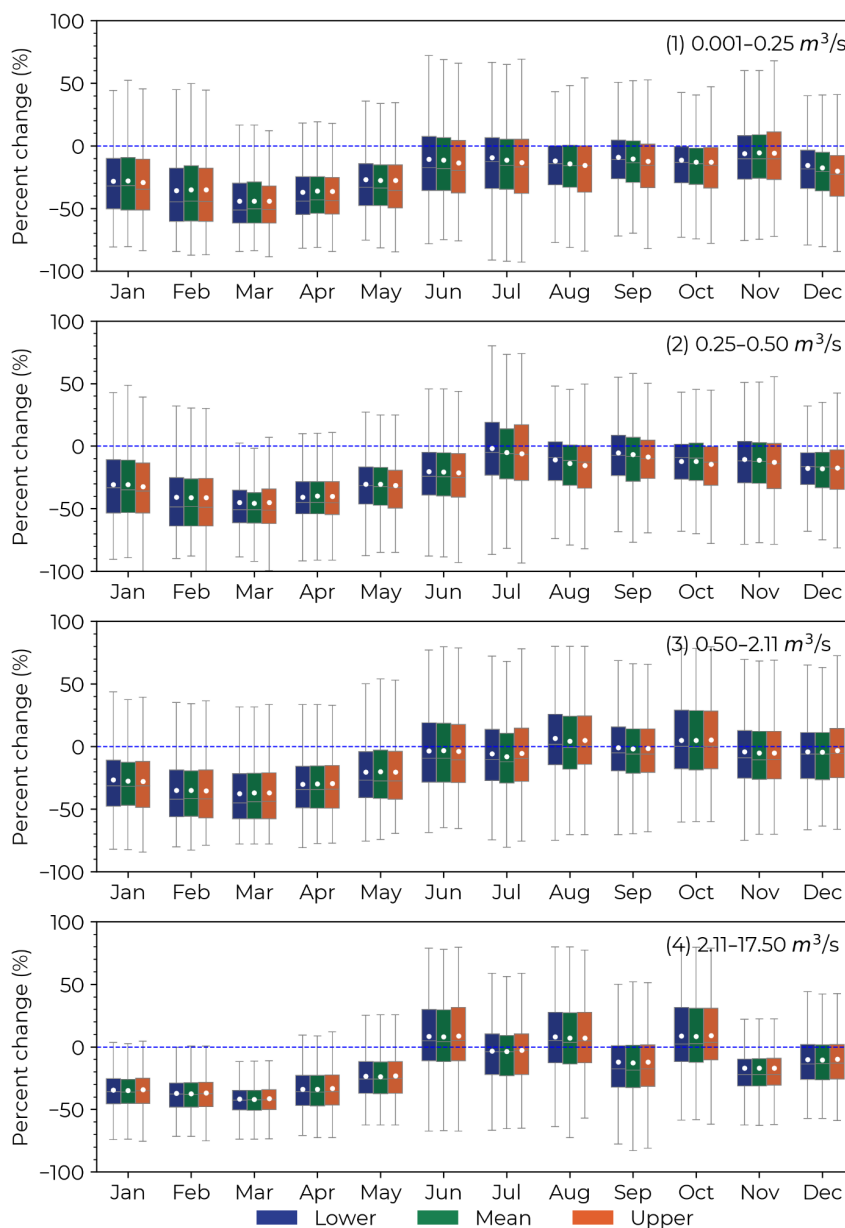
358 **Figure 4**—OFRs surface area distribution for the three surface area scenarios, lower, mean,
359 and upper.

360 The impact of the OFRs on monthly flow varied throughout the year, and the largest
361 impacts occurred between January and May for all flow classes (Fig. 5). During these months,
362 including all surface area scenarios, the mean decrease in flow (i.e., negative mean percent
363 change) was $-34.4 \pm 6\%$ for class 1, $-37.6 \pm 5\%$ for class 2, $-30.0 \pm 6\%$ for class 3, and $-34.1 \pm 6\%$ for
364 class 4. For all classes, the greatest reduction in flow occurred during the month of March (\sim -
365 40%). Meanwhile, the impact of the OFRs was smaller during the second half of the year, in
366 which the mean percent change in flow was $-12.0 \pm 3\%$ for class 1, $-12.5 \pm 5\%$ for class 2, $-1.4 \pm 4\%$
367 for class 3, and $-2.6 \pm 10\%$ for class 4 (Fig. 5). So we always saw a decrease? It looks like we have
368 some increases too.

369 When assessing the mean percent change per month, for all surface area scenarios,
370 the lower flow classes (i.e., (1) $0.001\text{--}0.25\text{ m}^3/\text{s}$ and (2) $0.25\text{--}0.50\text{ m}^3/\text{s}$) had a negative mean
371 percent change for all months. Nonetheless, we observed a mean positive percent change (i.e.,
372 increase in flow) for the months of August ($5.0 \pm 1\%$) and October ($5.2 \pm 0.2\%$) for class 3, and
373 during June ($8.2 \pm 0.3\%$), August ($7.3 \pm 0.4\%$), and October ($8.7 \pm 0.4\%$) for class 4 (Fig. 5).
374 Furthermore, the different surface area scenarios had similar impacts on flow for all months of
375 the year with differences smaller than 5% for all scenarios. Between January and May, for all
376 flow classes, the mean percent change was $-32.0 \pm 6\%$ for the lower, $-34.6 \pm 7\%$ for the mean,
377 and $-35.8 \pm 5\%$ for the upper. Between June and December, the impact on flow was $-5.4 \pm 6\%$
378 for the lower, $-7.3 \pm 8\%$ for the mean, and $-8.9 \pm 5\%$ for the upper.

379

380



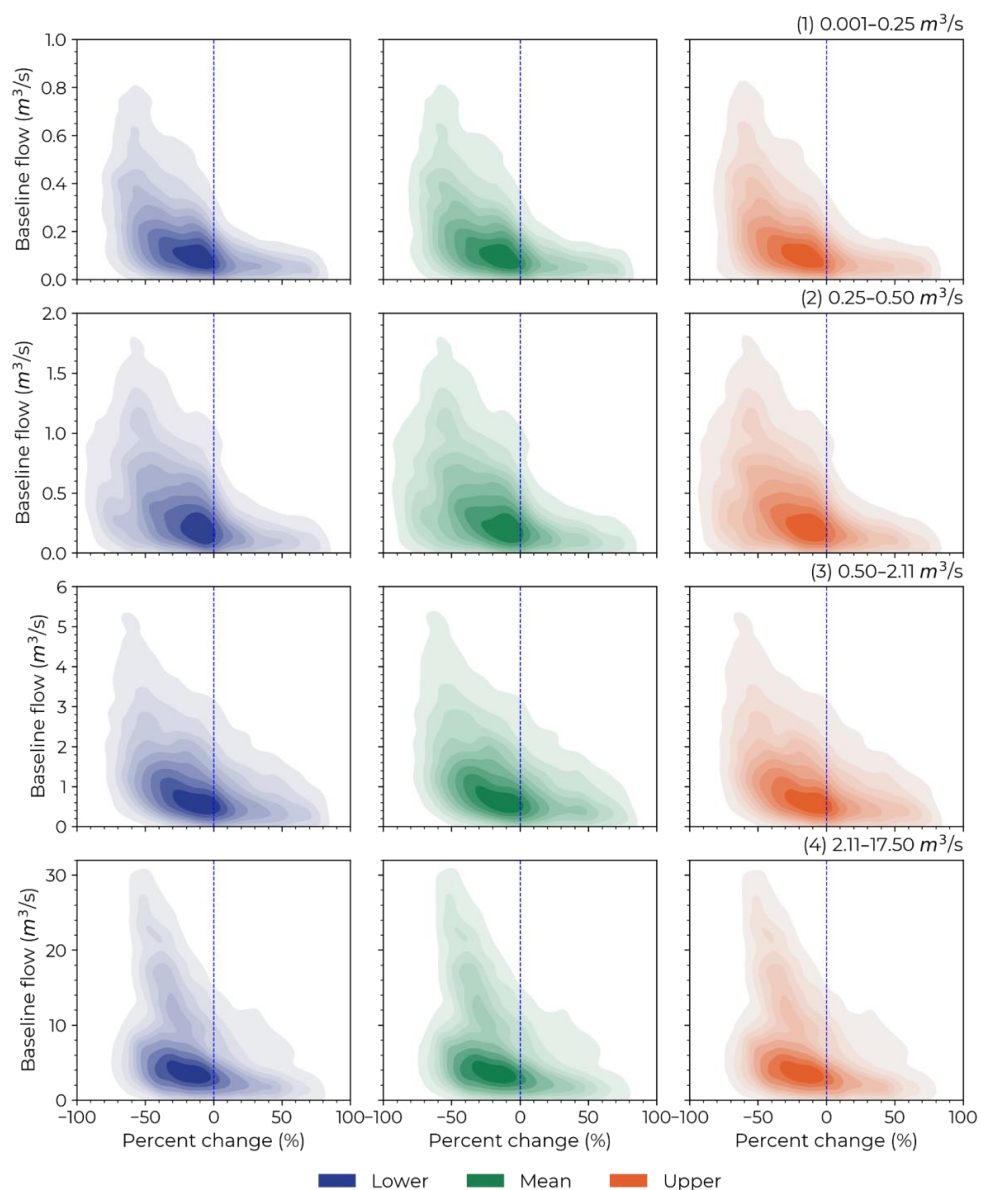
381
382 **Figure 5**—Monthly percent change in flow between the baseline scenario (vertical dotted blue
383 line) and the three surface area scenarios (lower, mean, and upper), and for the four flow classes
384 (1) 0.001–0.25 m³/s, (2) 0.25–0.50 m³/s, (3) 0.50–2.11 m³/s, and (4) 2.11–17.50 m³/s.



385 In general, the OFRs contributed to decreased monthly flow. However, the OFRs'
386 impact on flow had a significant intra- and inter-annual variability, and it varied according to
387 different OFRs and channels—this is highlighted by the boxplots size variability in Fig. 5, in
388 which the variability was lower during the first part of the year, and greater between July and
389 August. In addition, the monthly percent change in flow in the KDE plots (Fig. 6) shows that
390 for the three scenarios, and all flow classes, most of the changes in flow ranged between -40%
391 and 0%. In addition, all KDE plots have a triangular shape with its base on the smaller flows,
392 denoting where most of the changes occur. Even though the majority of the percent change
393 in flow is negative, there are circumstances in which the OFRs could positively impact flow—
394 the increase in flow is represented by faded colors in each surface area scenario (Fig. 6). The
395 positive mean percent change could be as high as 80%—see Fig. 6 for the larger flow classes,
396 (3) 0.50–2.11 m³/s and (4) 2.11–17.50 m³/s. The positive impact on flow for these classes occurred
397 during the months of June, August and October when a mean positive change is observed
398 (Fig. 5 classes 3 and 4).

399 The annual mean percent change, for all surface area scenarios, was $-22.5 \pm 3\%$ for class
400 1, $-24.2 \pm 4\%$ for class 2, $-14.6 \pm 3\%$ for class 3, and $-16.6 \pm 3\%$ for class 4. In addition, the surface
401 area scenarios annual changes were $-18.0 \pm 5\%$ for the lower, $-19.6 \pm 5\%$ for the mean, and -20.8
402 $\pm 6\%$ for the upper, including all flow classes. The differences between the surface area
403 scenarios shown in Fig. 5 and Fig. 6 are related to the variability of the OFRs surface area.

404
405
406
407



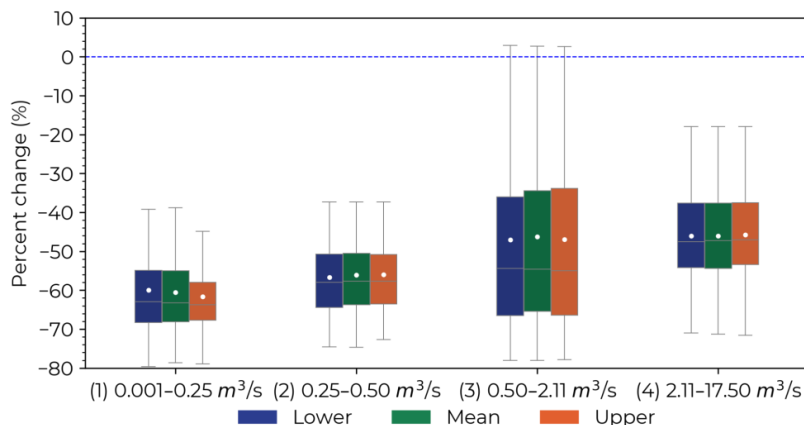
408

409 **Figure 6**–Kernel density estimation plots smoothed using a Gaussian kernel for the monthly
410 percent change in flow between the baseline scenario (vertical dotted blue line) and the three
411 surface area scenarios (lower, mean, and upper) for the four flow classes (1) 0.001–0.25 m³/s, (2)
412 0.25–0.50 m³/s, (3) 0.50–2.11 m³/s, and (4) 2.11–17.50 m³/s. Note the different range of values on
413 the y-axis for all four flow classes.



414 3.3 Impact on peak flow

415 For each channel, we calculated the impact of the OFRs on peak flow (Fig. 7). The impact on
416 peak flow was $-60.7 \pm 13\%$ for class 1, $-56.2 \pm 11\%$ for class 2, $-46.7 \pm 19\%$ for class 3, and $-43.9 \pm 12\%$
417 class 4. When assessing the impact on peak flow based on different surface area scenarios, the
418 mean percent change was $-49.4 \pm 18\%$ for the lower, $-50.4 \pm 17\%$ for the mean, and $-52.7 \pm 18\%$
419 for the upper. All peak flows occurred between January and May, which is the period of the
420 year when the study region receives most of its precipitation (Perin et al., 2021). With the
421 exception of a few outliers, there was no increase in peak flow, even though the OFRs
422 contributed to a positive mean percent change in flow in certain months of the year (Fig. 5
423 classes 3 and 4).



424

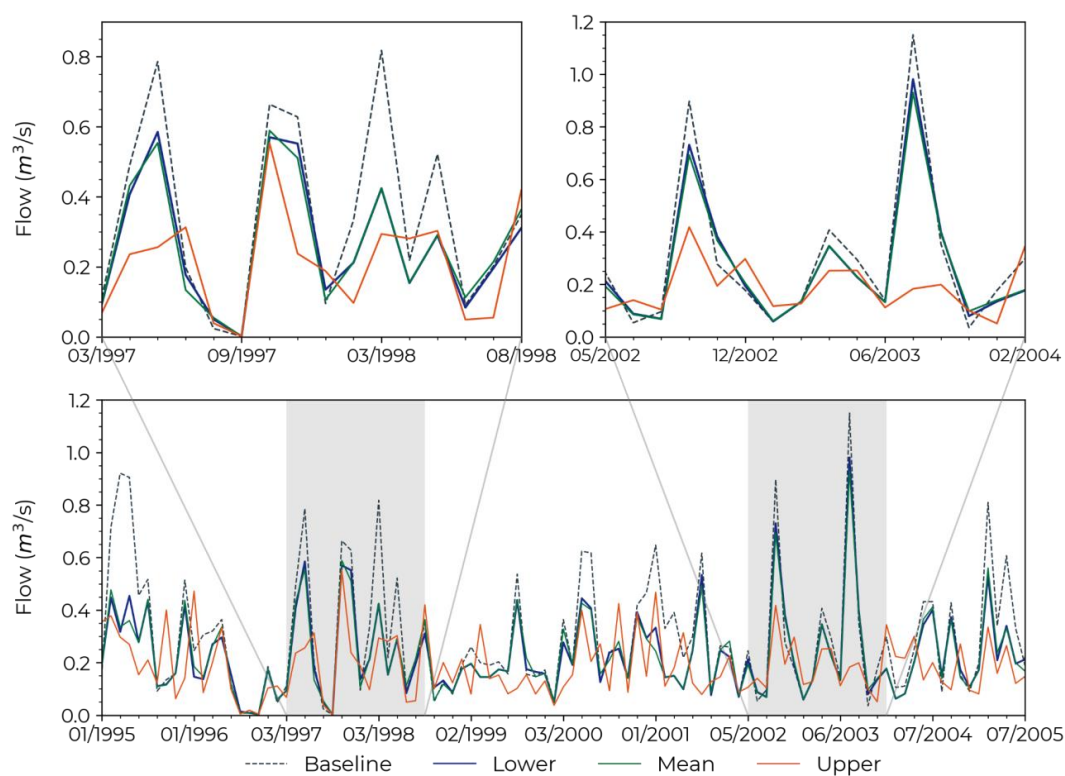
425 **Figure 7**—Percent change in peak flow between the baseline scenario (vertical dotted blue line)
426 and the three surface area scenarios (lower, mean, and upper) for the four flow classes (1) 0.001–
427 0.25 m³/s, (2) 0.25–0.50 m³/s, (3) 0.50–2.11 m³/s, and (4) 2.11–17.50 m³/s.

428 3.4 Simulated flow time series

429 We randomly selected a channel within the flow class 3 to demonstrate the baseline and the
430 three surface area scenarios' flow time series between 1995 and 2005 (Fig. 8). For this channel,
431 the annual mean percent changes in flow when comparing the baseline scenario with the
432 lower, mean, and upper surface area scenarios were $0.99 \pm 11.8\%$, $-1.9 \pm 13\%$, and $-2.0 \pm 19\%$ —the



433 high standard deviation for the three scenarios is explained by the interannual variability. The
434 upper surface area scenario resulted in lower flows (i.e., higher impact) when compared to the
435 lower and mean scenarios for the majority of the flow events—67.8% and 57.6% for the lower
436 and mean scenarios. Nonetheless, there are circumstances when the upper scenario yielded
437 higher flows—32.2% and 42.4% of the events for the lower and mean scenarios (e.g., see the
438 two insets 03/1997–08/1998 and 05/2002–02/2004). These findings indicate that the impacts
439 that the OFRs have on flow are not entirely governed by the presence and surface area of the
440 OFRs (i.e., the different surface area scenarios), instead by a combination of the OFRs with
441 different modeling components (e.g., terrain, land use, climate information), and different
442 hydrological processes (e.g., run-off, precipitation, evaporation). In addition, the impact on
443 peak flow for this channel was $-45.7 \pm 19.7\%$ for all surface area scenarios—this is highlighted
444 on two occasions (08/2002 and 08/2003) during the second inset.



445



446 **Figure 8**–A subset of the time series of simulated flow for baseline and the three surface area
447 scenarios (lower, mean, and upper) between 1995 and 2005 for a selected channel within the
448 flow class 3.

449

450

451

452

453

454

455

456

457



468 To assess the overall impact of the OFRs at the subwatershed level, we calculated the
469 contribution of each subwatershed flow to the main model outlet, and the subwatersheds'
470 reservoir capacity (i.e., summing the OFRs surface area at each subwatershed and dividing it
471 to the total OFRs surface area, including all OFRs from all subwatersheds) (Fig. 9). In general,
472 the highest impacts on annual flow (e.g., > 100%), with positive or negative magnitude,
473 occurred at the subwatersheds that contributed the least (< 10%) to the main model outlet—
474 these subwatersheds are represented in lighter shades of blue, and the annual impact is
475 highlighted in yellow on Fig. 9. In other words, the highest impacts on flow occurred on the
476 channels with smaller flow magnitudes (e.g., channels that presented mean flow ranging
477 between 0.001–0.25 and 0.25–0.50 m³/s, these channels were classified as class 1 and 2 in this
478 study). In addition, the subwatersheds with the highest reservoir capacities (between 15.3 and
479 19.1 %, represented in darker shades of blue) (Fig. 9), had a small (< 10%) contribution to the
480 model outlet, and these subwatersheds did not present the highest impact on annual flow
481 (e.g., the impact on annual flow for the top two subwatersheds in terms of reservoir capacity
482 were -0.9 and 82.1%).

483



484 4 Discussion

485 Although OFRs will contribute to improve food production resilience—by providing surface
486 water to irrigation during dry periods—to severe drought events, which are expected to have
487 higher occurrence with climate change, OFRS can have cumulative impacts on surface
488 hydrology of the watershed where they occur. Studies have either used data driven or
489 physically based hydrological model approaches to estimate OFR impacts on the watersheds,
490 despite the fact that combining the two approaches leads to better understanding on what is
491 the spatial and temporal variability of the OFR impacts, given that the dynamic changes of the
492 OFRs are incorporated into the hydrological model. To quantify whether the impact of the
493 OFRS on mean and peak flow varied intra- and inter-annually, and which subwatersheds are
494 more impacted, here we combined a data-driven remote sensing-based model with SWAT+
495 latest improvements to assess the OFR impacts.

496 4.1 Cumulative impact of OFRs

497 When simulating water impoundments in SWAT/SWAT+, it is common practice to
498 validate and calibrate the model using flow measurements (Evenson et al., 2018; Habets et al.,
499 2018; Jalowska & Yuan, 2019; Ni & Parajuli, 2018). In addition, other studies have validated and
500 calibrated the model using alternative variables. For example, Perrin et al., (2012) employed
501 monthly measurements of piezometric variations to assess aquifer recharge processes, and
502 Jalowska & Yuan (2019) used sediment loadings (concentration and budget), from field
503 monitoring reports to evaluate sediment simulations. Ideally, we would calibrate and validate
504 the model by accounting for the parameters governing the OFRs' water budget (e.g., inflows
505 and outflows) (e.g., Kim and Parajuli, 2014). Nonetheless, these measurements were not
506 available for the OFRs in our study region. Furthermore, a thorough calibration and validation
507 of the model would require extra flow data, covering other parts of the study region, as the
508 three USGS stations—the only data available—used in this study are located in the upper part



509 of the modeled watershed. Similar to Evenson et al., (2018)—who proposed a module to better
510 represent spatially distributed wetlands, and validated their model using a direct (i.e., flow
511 measurement) and an indirect (i.e., the wetlands surface area) approach—our validation and
512 calibration was done using the flow measurements, and the OFRs surface area scenarios were
513 based on an algorithm that was validated with an independent higher spatial resolution
514 dataset (Perin et al., 2022).

515 There is a consensus within the scientific community that the OFRs will have a
516 cumulative impact on surface hydrology by decreasing flow and peak flow, and the impact will
517 vary from watershed to watershed due to the number of OFRs, and the OFRs' different
518 purposes (e.g., different irrigation schedule) (Ayalew et al., 2017; Fowler et al., 2015; Habets et al.,
519 2018; Nathan & Lowe, 2012; Pinhati et al., 2020; Rabelo et al., 2021). As pointed out by Habets et
520 al., (2018) the mean annual decrease in flow from all studies was $-13.4\% \pm 8\%$. Our results are
521 aligned with this value, which varied between $-24.2 \pm 4\%$ and $-14.6 \pm 3\%$ for all flow classes. In
522 addition, OFRs can reduce peak flow on average by 45% (Habets et al., 2018; Nathan and Lowe,
523 2012; Thompson, 2012), and up to 70% (Ayalew et al., 2017) for certain flow events. Likewise, our
524 results are consistent with these findings, in which the mean impact on peak flow varied
525 between $-60.7 \pm 12\%$ and $-43.9 \pm 12\%$. Furthermore, differently from previous research, our
526 results showed that the OFRs may have a positive ($< 9\%$) impact on flow (Fig. 5, classes 3 and
527 4). This could be explained by the level of details in our analyses. While we calculated the
528 monthly impact on flow at the channel scale by aggregating the OFRs to the closest channel,
529 previous studies have mostly reported the annual impact on flows (Habets et al., 2018), and
530 they performed their analysis at the subwatershed scale by aggregating the OFRs to a single
531 point at the outlet of each subwatershed in SWAT (Evenson et al., 2018; Kim & Parajuli, 2014;
532 Perrin, 2012; Zhang et al., 2012), or they used different modeling approaches (see Habet et al.,
533 (2018)).

534 By leveraging the latest improvements in SWAT+ to simulate water impoundments
535 (Molina-Navarro et al., 2018) in combination with a novel algorithm to monitor OFRs (Perin et



536 al., 2022), we modeled the impact of the OFRs on flow at the channel scale. In addition, the
537 surface area scenarios enabled us to account for events when the OFRs were at the lowest,
538 regular, and fullest capacities according to their surface area (see Fig. 2). This is an
539 improvement over previous studies (e.g., Ni et al., 2020; Ni and Parajuli, 2018; Perrin, 2012) that
540 used a single surface area (i.e., one snapshot in time) to represent the OFRs in SWAT. The small
541 differences ($< 5\%$) between the surface area scenarios in terms of mean percent change on
542 monthly flow indicates that the OFRs' surface area variation had a low impact on flow. For
543 instance, during January and May the mean monthly percent change ranged between $-35.8 \pm$
544 6% and $-32.0 \pm 7\%$, and during June and December it varied between $-8.8 \pm 5\%$ and $-5.4 \pm 6\%$
545 for the three surface area scenarios. The same was observed for peak flow, with a mean
546 monthly impact ranging between $-52.7 \pm 17\%$ and $-49.4 \pm 18\%$. This small variability on flow
547 impact was observed even though the total OFR surface area increased by 590 ha and 1194 ha
548 when comparing the lower scenario with the mean and upper scenarios (Fig. 5). However, the
549 OFRs represented a small portion ($< 1\%$) of the total area of the modeled watershed (Fig. 1).
550 These findings are related to the fact that flow simulations are governed by several
551 hydrological processes (e.g., run-off, precipitation, evapotranspiration) besides the presence of
552 OFRs on the channel (Bieger et al., 2017; Dile et al., 2022; Arnold et al., 2012). In addition, when
553 assessing the percent change in flow at the channel scale, the differences in surface area
554 between the scenarios occurred at a lower magnitude when compared to the total OFRs
555 surface area. For instance, an OFR with surface area smaller than 10 ha, and with surface area
556 variations between 10 and 20% for the three scenarios, may not lead to differences (e.g., $> 10\%$)
557 between the three scenarios.

558 4.2 OFRs impacts on flow and peak flow

559 Our findings highlight that the impacts of the OFRs on flow and peak flow have a
560 significant intra- and inter-annual variability (Figs. 5, 6, and 7), and the impacts vary according
561 to different OFRs and channels (Fig. 5). The largest impacts on flow occurred during the first



562 part of the year between January and May, the period of the year when the peak flows occur.
563 In addition, this time of the year also coincides with the period when the region receives most
564 of its precipitation (Perin et al., 2021b), and the OFRs are at their fullest capacity (i.e., OFRs
565 storing their maximum amount of water) (Perin et al., 2022). During the second part of the year,
566 we observed a milder mean percent change in flow for all flow classes and all scenarios, and a
567 greater variability in percent change, notably for the months of July and August (Fig. 5).
568 Moreover, most of the irrigation activities happen between June and September (Perin et al.,
569 2021b, Yaeger et al., 2017), and it is when the OFRs are at their lowest capacities (i.e., storing less
570 water) (Perin et al., 2022), which could explain their moderate impact and higher variability
571 during these months—even though we are not accounting for the OFRs inflows and outflows,
572 and not simulating irrigation events. Additionally, the variability of the OFRs impacts is related
573 to the OFRs' physical properties (e.g., surface area and location in the watershed). For example,
574 the OFR surface area will have an impact on flow and peak flow, as shown by the different
575 surface area scenarios, and depending on where the OFR is located in the watershed, given
576 that it may be connected to lower or higher flow channels, which contributes to their impact
577 variability during the year (Figs. 4 and 5). Besides the OFRs' physical properties, the built-in
578 complexity of SWAT—when simulating the presence of the OFRs and the various hydrological
579 processes (e.g., run-off, precipitation, evapotranspiration) governing the water cycle—
580 contributes to the differences in the OFRs impacts. This complexity is illustrated in Fig. 8
581 showing that the upper scenario can have a higher or lower impact on flow when compared
582 to the lower and mean scenarios.

583 When assessing the annual impact of the OFRs accounting for each subwatershed flow
584 compared to the main model outlet flow, and each subwatershed reservoir capacity (Fig. 9),
585 we found that even though the presence of the OFRs can have a significant impact on flow
586 (Figs. 5, 6, and 7), the highest impacts tend to occur on the subwatersheds that contribute the
587 least (< 10%) to the main model outlet. In general, the highest impacts occurred on the



588 channels with smaller flow magnitudes, and the subwatersheds with the highest reservoir
589 capacities did not have the highest impact on flow.

590 4.3 Research implications and applications to other study regions

591 Overall, we presented a new approach to quantitatively analyze the impact of a network
592 of OFRs on mean and peak flow, and we described the various potential reasons behind the
593 variability of the impacts. Our results indicate that OFRs do not have an equally distributed
594 impact on mean and peak flow across the watershed. Hence, assessing the OFRs location as
595 well as their numbers across the watershed is important when aiming to manage the
596 construction of new OFRs. In particular, the geospatial variability of the OFRs impacts could be
597 taken into account by water agencies when planning and developing a network of OFRs, given
598 it is possible to identify the areas that are under high pressure (e.g., regions with multiple OFRs
599 that are having a significant impact on flow), and to identify areas that could benefit from the
600 construction of new OFRs, targeting improvements on water resources management and
601 irrigation activities.

602 Furthermore, even though the OFRs impacts may vary significantly in different
603 watersheds (Habets et al., 2018), our approach could be transferable to other places across the
604 world, as it integrates a top-down data-driven remote sensing-based algorithm, which is
605 based on freely available and private Earth Observations datasets, with the latest SWAT+
606 hydrological modeling developments. In addition, the widespread use of SWAT+ and its open-
607 source nature, is yet another factor contributing to the transferability of the novel approach
608 presented in this study. This is relevant as the number of OFRs is expected to increase globally
609 (Althoff et al., 2020; Habets et al., 2014; Habets et al., 2018; Krol et al., 2011; Rodrigues et al., 2012),
610 with a limited knowledge of how the OFRs may impact surface hydrology in different
611 watersheds, and under diverse environmental conditions. Finally, in tandem with the OFRs'
612 key role on irrigated food production, in part to adapt to climate change (Habets et al., 2018)
613 and to alleviate the pressure on surface and groundwater resources (Vanthof & Kelly, 2019;



614 Yaeger et al., 2017; Yaeger et al., 2018), their impacts on surface hydrology need to be
615 considered to avoid exacerbating the surface water stress already intensified by climate
616 change and population growth (Vörösmarty et al., 2010).

617 5 Future improvements

618 Future improvements should focus on how to better represent the OFRs water management
619 (i.e., OFRs inflows and outflows) in SWAT+. Given that each OFR has an independent water
620 balance, accounting for the OFRs water volume change would be a more realistic
621 representation of the OFRs when compared to the three surface area scenarios tested in this
622 study. Estimating the OFRs volume change can be done by combining the OFRs surface area
623 time series with area-elevation equations—these equations describe the OFRs' bathymetry,
624 and allow volume estimation by inputting the OFRs' surface area (Liebe et al., 2005; Meigh,
625 1995; Sawunyama et al., 2006). After carefully assessing different methods to derive these
626 equations (Arvor et al., 2018; Avisse et al., 2017; Li et al., 2021; Meigh, 1995; Sawunyama et al., 2006;
627 Vanthof & Kelly, 2019; Yao et al., 2018; Zhang et al., 2016), we decided that measured ground-
628 data of the OFRs' depth—which is not available—is required to estimate the equations with an
629 acceptable uncertainty. Estimating the area-elevation equations entails several challenges,
630 including: 1) despite the fact that there are several DEMs available for the study region
631 (Arkansas GIS Office, 2022)—DEMs can be used to estimate the OFRs bottom elevation—the
632 DEMs were collected when most of the OFRs were full (i.e., bathymetry was not exposed),
633 which limits their use in this case; and 2) although the OFRs are located within the same
634 geomorphological region, they have different depth, shape and physical characteristics (Perin
635 et al., 2022; Yaeger et al., 2017). Therefore, even if a generalized area-elevation equation was
636 calculated for our study region—this is a common approach done by other studies (Mady et
637 al., 2020; Vanthof and Kelly, 2019)—that would still lead to high uncertainties of water volume
638 changes. Ideally, each OFR would have its own equation, which was not possible when this
639 study was done.



640 Efforts should also be made to improve SWAT+ capabilities to receive measured OFRs'
641 inflows and outflows. The latest version of the model has improved the hydrological
642 representation of small water impoundments in SWAT+ (Mollina-Navarro et al., 2018).
643 Nonetheless, at the time of our study, the newest version of the model does not allow users to
644 input measured or calculated OFRs' inflows and outflows. Instead, the model developers
645 recommend simulating the OFRs water balance using decision tables (Arnold et al., 2018; Dile
646 et al., 2022). However, there are very limited guidelines on how to create these decision tables.
647 In addition, the tables would simulate the OFRs water balance instead of using the measured
648 or calculated volume change, which could introduce more uncertainties to the modeling
649 scenarios.

650 6 Conclusions

651 We proposed a novel approach that combines a top-down data driven remote sensing-based
652 algorithm with the latest developments in SWAT+ to simulate the cumulative impacts of OFRs.
653 This enabled us to assess the spatial and temporal variability of the OFRs impacts, as well as
654 the intra- and inter-annual impact changes on mean and peak flow, at the watershed and
655 subwatershed levels. Incorporating Earth Observation derived information with a hydrological
656 model, allowed us to capture the dynamic changes of the OFRs, and to simulate their impacts
657 under different OFR capacity scenarios.

658 Our study showed that the OFRs may have an impact on flow and peak flow, which can
659 have a significant inter- and intra-annual variability. The impact of the OFRs is not equally
660 distributed across the watershed, and it varies according to the OFRs spatial distribution, and
661 their surface area (i.e., water storage capacity). As the number of OFRs is expected to increase
662 globally—partially to adapt to climate change and to alleviate pressure on groundwater
663 resources—and therefore, also increase their relevance to irrigated food production, it is
664 imperative to develop new frameworks to further understand the OFRs impacts on surface
665 hydrology. In this regard, we provided a combination of different methods that can be used in



666 other watersheds, which can support water agencies with information to improve surface
667 water resources management.

668 7 Author contribution

669 VP, MGT planned study, analyzed data and modeling, and wrote and reviewed the
670 manuscript. SF and AS carried out software analyses, wrote and reviewed. MLR and MAY data
671 curation, wrote and reviewed.

672 8 Competing interests

673 The contact author has declared that none of the authors has any competing interests.

674 9 Acknowledgments

675 The first author was supported by NASA through the Future Investigators in NASA Earth and
676 Space Science and Technology fellowship.

677 10 Data Availability

678 The Soil Water Assessment Tool (SWAT) hydrological model and all necessary tools to
679 perform calibration, validation, and data analyses can be accessed through SWAT's online
680 portal: <https://swat.tamu.edu/>.

681
682 The National Land Cover Database (30 m) (Homer et al., 2020) and the Gridded Soil Survey
683 Geographic Database (gSSURGO) (Soil Survey Staff, USDA-NRCS, 2021) (100 m) are accessible
684 through the USGS's portal: [https://www.usgs.gov/centers/eros/science/national-land-cover-](https://www.usgs.gov/centers/eros/science/national-land-cover-database)
685 [database](https://www.nrcs.usda.gov/resources/data-and-reports/gridded-soil-survey-geographic-gssurgo-database), and here [https://www.nrcs.usda.gov/resources/data-and-reports/gridded-soil-](https://www.nrcs.usda.gov/resources/data-and-reports/gridded-soil-survey-geographic-gssurgo-database)
686 [survey-geographic-gssurgo-database](https://www.nrcs.usda.gov/resources/data-and-reports/gridded-soil-survey-geographic-gssurgo-database), respectively.

687
688 The climate data extracted from the Gridded Surface Meteorological Datasets (Abatzoglou,
689 2013) is available in Google Earth Engine (Gorelick et al., 2017), here
690 https://developers.google.com/earth-engine/datasets/catalog/IDAHO_EPSCOR_GRIDMET.

691
692 The Kalman filter derived surface area time series is available through Perin et al., (2022).

693 10 References

- 694
695 Abatzoglou, J. T.: Development of gridded surface meteorological data for ecological
696 applications and modelling, *Int. J. Climatol.*, 33, 121–131, <https://doi.org/10.1002/joc.3413>, 2013.
697
698 Althoff, D., Rodrigues, L. N., and da Silva, D. D.: Impacts of climate change on the evaporation
699 and availability of water in small reservoirs in the Brazilian savannah, *Clim. Change*, 159, 215–
700 232, <https://doi.org/10.1007/s10584-020-02656-y>, 2020.
701
702 Arkansas GIS Office: Arkansas GIS Office | Elevation datasets, 2022.



- 703 Arnold, J. G., Moriasi, D. N., Gassman, P. W., Abbaspour, K. C., M. J. White, M. J., Srinivasan, R.,
704 Santhi, C., Harmel, R. D., van Griensven, A., Van Liew, M. W., Kannan, N., and Jha, M. K.: SWAT:
705 Model Use, Calibration, and Validation, *Trans. ASABE*, 55, 1491–1508,
706 <https://doi.org/10.13031/2013.42256>, 2012.
707
- 708 Arnold, J. G., Bieger, K., White, M. J., Srinivasan, R., Dunbar, J. A., and Allen, P. M.: Use of
709 Decision Tables to Simulate Management in SWAT+, *Water*, 10, 713,
710 <https://doi.org/10.3390/w10060713>, 2018.
711
- 712 Arvor, D., Daher, F. R. G., Briand, D., Dufour, S., Rollet, A.-J., Simões, M., and Ferraz, R. P. D.:
713 Monitoring thirty years of small water reservoirs proliferation in the southern Brazilian
714 Amazon with Landsat time series, *ISPRS J. Photogramm. Remote Sens.*, 145, 225–237,
715 <https://doi.org/10.1016/j.isprsjprs.2018.03.015>, 2018.
716
- 717 Avisse, N., Tilmant, A., Müller, M. F., and Zhang, H.: Monitoring small reservoirs' storage with
718 satellite remote sensing in inaccessible areas, *Hydrol. Earth Syst. Sci.*, 21, 6445–6459,
719 <https://doi.org/10.5194/hess-21-6445-2017>, 2017.
720
- 721 Ayalew, T. B., Krajewski, W. F., Mantilla, R., Wright, D. B., and Small, S. J.: Effect of Spatially
722 Distributed Small Dams on Flood Frequency: Insights from the Soap Creek Watershed, *J.*
723 *Hydrol. Eng.*, 22, 04017011, [https://doi.org/10.1061/\(ASCE\)HE.1943-5584.0001513](https://doi.org/10.1061/(ASCE)HE.1943-5584.0001513), 2017.
724
- 725 Bieger, K., Arnold, J. G., Rathjens, H., White, M. J., Bosch, D. D., Allen, P. M., Volk, M., and
726 Srinivasan, R.: Introduction to SWAT+, A Completely Restructured Version of the Soil and
727 Water Assessment Tool, *JAWRA J. Am. Water Resour. Assoc.*, 53, 115–130,
728 <https://doi.org/10.1111/1752-1688.12482>, 2017.
729
- 730 Canter, L. W. and Kamath, J.: Questionnaire checklist for cumulative impacts, *Environ. Impact*
731 *Assess. Rev.*, 15, 311–339, [https://doi.org/10.1016/0195-9255\(95\)00010-C](https://doi.org/10.1016/0195-9255(95)00010-C), 1995.
732 Chalise, D. R., Sankarasubramanian, A., and Ruhí, A.: Dams and Climate Interact to Alter River
733 Flow Regimes Across the United States, *Earth's Future*, 9,
734 <https://doi.org/10.1029/2020EF001816>, 2021.
735
- 736 SWAT+ Toolbox: <https://celray.github.io/docs/swatplus-toolbox/v1.0/index.html>, last access: 17
737 June 2022.
738
- 739 Chawanda, C. J., Arnold, J., Thiery, W., and van Griensven, A.: Mass balance calibration and
740 reservoir representations for large-scale hydrological impact studies using SWAT+, *Clim.*
741 *Change*, 163, 1307–1327, <https://doi.org/10.1007/s10584-020-02924-x>, 2020.
742
- 743 Culler, R. C., Hadley, R. F., and Schumm, S. A.: Hydrology of the upper Cheyenne River basin:
744 Part A. Hydrology of stock-water reservoirs in upper Cheyenne River basin; Part B. Sediment
745 sources and drainage-basin characteristics in upper Cheyenne River basin, U.S. Geological
746 Survey, <https://doi.org/10.3133/wsp1531>, 1961.
747
- 748 Dile, Y., Srinivasan, R., and George, C.: QGIS Interface for SWAT+: QSWAT+, 2022.
749
- 750 Döll, P., Fiedler, K., and Zhang, J.: Global-scale analysis of river flow alterations due to water
751 withdrawals and reservoirs, *Hydrol. Earth Syst. Sci.*, 13, 2413–2432, <https://doi.org/10.5194/hess-13-2413-2009>, 2009.
752
- 753
- 754 Downing, J. A.: Emerging global role of small lakes and ponds: little things mean a lot,
755 *Limnetica*, 29, 9–24, <https://doi.org/10.23818/limn.29.02>, 2010.



- 756 Dubreuil, P. and Girard, G.: Influence of a very large number of small reservoirs on the annual
757 flow regime of a tropical stream, *Wash. DC Am. Geophys. Union Geophys. Monogr. Ser.*, 17,
758 295–299, 1973.
- 759
760 Irrigation & Water Use: [https://www.ers.usda.gov/topics/farm-practices-](https://www.ers.usda.gov/topics/farm-practices-management/irrigation-water-use/)
761 [management/irrigation-water-use/](https://www.ers.usda.gov/topics/farm-practices-management/irrigation-water-use/), last access: 30 October 2021.
- 762
763 Entekhabi, D., Njoku, E. G., O'Neill, P. E., Kellogg, K. H., Crow, W. T., Edelstein, W. N., Entin, J. K.,
764 Goodman, S. D., Jackson, T. J., Johnson, J., Kimball, J., Piepmeier, J. R., Koster, R. D., Martin, N.,
765 McDonald, K. C., Moggaddam, M., Moran, S., Reichle, R., Shi, J. C., Spencer, M. W., Thurman, S.
766 W., Tsang, L., and Van Zyl, J.: The Soil Moisture Active Passive (SMAP) Mission, *Proc. IEEE*, 98,
767 704–716, <https://doi.org/10.1109/JPROC.2010.2043918>, 2010.
- 768
769 Evenson, G. R., Jones, C. N., McLaughlin, D. L., Golden, H. E., Lane, C. R., DeVries, B., Alexander,
770 L. C., Lang, M. W., McCarty, G. W., and Sharifi, A.: A watershed-scale model for depressionnal
771 wetland-rich landscapes, *J. Hydrol. X*, 1, 100002, <https://doi.org/10.1016/j.hydroa.2018.10.002>,
772 2018.
- 773
774 Farr, T. G., Rosen, P. A., Caro, E., Crippen, R., Duren, R., Hensley, S., Kobrick, M., Paller, M.,
775 Rodriguez, E., Roth, L., Seal, D., Shaffer, S., Shimada, J., Umland, J., Werner, M., Oskin, M.,
776 Burbank, D., and Alsdorf, D.: The Shuttle Radar Topography Mission, *Rev. Geophys.*, 45,
777 <https://doi.org/10.1029/2005RG000183>, 2007.
- 778
779 Fowler, K., Morden, R., Lowe, L., and Nathan, R.: Advances in assessing the impact of hillside
780 farm dams on streamflow, *Australas. J. Water Resour.*, 19, 96–108,
781 <https://doi.org/10.1080/13241583.2015.1116182>, 2015.
- 782
783 Galéa, G., Vasquez-Paulus, B., Renard, B., and Breil, P.: L'impact des prélèvements d'eau pour
784 l'irrigation sur les régimes hydrologiques des sous-bassins du Tescou et de la Séoune (bassin
785 Adour-Garonne, France), *Rev. Sci. Eau J. Water Sci.*, 18, 273–305,
786 <https://doi.org/10.7202/705560ar>, 2005.
- 787
788 George, C.: Using SSURGO soil data with QSWAT and QSWAT+, 2020.
- 789 Gorelick, N., Hancher, M., Dixon, M., Ilyushchenko, S., Thau, D., and Moore, R.: Google Earth
790 Engine: Planetary-scale geospatial analysis for everyone, *Remote Sens. Environ.*, 202, 18–27,
791 <https://doi.org/10.1016/j.rse.2017.06.031>, 2017.
- 792
793 Habets, F., Philippe, E., Martin, E., David, C. H., and Leseur, F.: Small farm dams: Impact on river
794 flows and sustainability in a context of climate change, *Hydrol. Earth Syst. Sci.*, 18, 4207–4222,
795 <https://doi.org/10.5194/hess-18-4207-2014>, 2014.
- 796
797 Habets, F., Molénat, J., Carluer, N., Douez, O., and Leenhardt, D.: The cumulative impacts of
798 small reservoirs on hydrology: A review, *Sci. Total Environ.*, 643, 850–867,
799 <https://doi.org/10.1016/j.scitotenv.2018.06.188>, 2018.
- 800
801 Homer, C., Dewitz, J., Jin, S., Xian, G., Costello, C., Danielson, P., Gass, L., Funk, M., Wickham, J.,
802 Stehman, S., Auch, R., and Riitters, K.: Conterminous United States land cover change
803 patterns 2001–2016 from the 2016 National Land Cover Database, *ISPRS J. Photogramm.*
804 *Remote Sens.*, 162, 184–199, <https://doi.org/10.1016/j.isprsjprs.2020.02.019>, 2020.
- 805
806 Hwang, J., Kumar, H., Ruhi, A., Sankarasubramanian, A., and Devineni, N.: Quantifying Dam-
807 Induced Fluctuations in Streamflow Frequencies Across the Colorado River Basin, *Water*
808 *Resour. Res.*, 57, <https://doi.org/10.1029/2021WR029753>, 2021.



- 809
810 Jalowska, A. M. and Yuan, Y.: Evaluation of SWAT Impoundment Modeling Methods in Water
811 and Sediment Simulations, *JAWRA J. Am. Water Resour. Assoc.*, 55, 209–227,
812 <https://doi.org/10.1111/1752-1688.12715>, 2019.
813
814 Jones, S. K., Fremier, A. K., DeClerck, F. A., Smedley, D., Pieck, A. O., and Mulligan, M.: Big data
815 and multiple methods for mapping small reservoirs: Comparing accuracies for applications in
816 agricultural landscapes, *Remote Sens.*, 9, <https://doi.org/10.3390/rs9121307>, 2017.
817
818 Justice, C. O., Vermote, E., Townshend, J. R. G., Defries, R., Roy, D. P., Hall, D. K., Salomonson, V.
819 V., Privette, J. L., Riggs, G., Strahler, A., Lucht, W., Myneni, R. B., Knyazikhin, Y., Running, S. W.,
820 Nemani, R. R., Zhengming Wan, Huete, A. R., van Leeuwen, W., Wolfe, R. E., Giglio, L., Muller, J.,
821 Lewis, P., and Barnsley, M. J.: The Moderate Resolution Imaging Spectroradiometer (MODIS):
822 land remote sensing for global change research, *IEEE Trans. Geosci. Remote Sens.*, 36, 1228–
823 1249, <https://doi.org/10.1109/36.701075>, 1998.
824
825 Kalman, R. E.: A new approach to linear filtering and prediction problems, 1960.
826 Kennon, F. W.: Hydrologic effects of small reservoirs in Sandstone Creek Watershed,
827 Beckham and Roger Mills Counties, western Oklahoma, U.S. G.P.O., 1966.
828 Khazaei, B., Read, L. K., Casali, M., Sampson, K. M., and Yates, D. N.: GLOBathy, the global lakes
829 bathymetry dataset, *Sci. Data*, 9, 36, <https://doi.org/10.1038/s41597-022-01132-9>, 2022.
830
831 Kim, H. K. and Parajuli, P. B.: Impacts of Reservoir Outflow Estimation Methods in SWAT
832 Model Calibration, *Trans. ASABE*, 1029–1042, <https://doi.org/10.13031/trans.57.10156>, 2014.
833
834 Krol, M. S., de Vries, M. J., van Oel, P. R., and de Araújo, J. C.: Sustainability of Small Reservoirs
835 and Large Scale Water Availability Under Current Conditions and Climate Change, *Water*
836 *Resour. Manag.*, 25, 3017–3026, <https://doi.org/10.1007/s11269-011-9787-0>, 2011.
837
838 Li, Y., Gao, H., Allen, G. H., and Zhang, Z.: Constructing Reservoir Area–Volume–Elevation Curve
839 from TanDEM-X DEM Data, *IEEE J. Sel. Top. Appl. Earth Obs. Remote Sens.*, 14, 2249–2257,
840 <https://doi.org/10.1109/JSTARS.2021.3051103>, 2021.
841
842 Liebe, J., van de Giesen, N., and Andreini, M.: Estimation of small reservoir storage capacities
843 in a semi-arid environment, *Phys. Chem. Earth*, 30, 448–454,
844 <https://doi.org/10.1016/j.pce.2005.06.011>, 2005.
845
846 Mady, B., Lehmann, P., Gorelick, S. M., and Or, D.: Distribution of small seasonal reservoirs in
847 semi-arid regions and associated evaporative losses, *Environ. Res. Commun.*, 2, 061002,
848 <https://doi.org/10.1088/2515-7620/ab92af>, 2020.
849
850 Meigh, J.: The impact of small farm reservoirs on urban water supplies in Botswana, *Nat.*
851 *Resour. Forum*, 19, 71–83, <https://doi.org/10.1111/j.1477-8947.1995.tb00594.x>, 1995.
852
853 Molina-Navarro, E., Nielsen, A., and Trolle, D.: A QGIS plugin to tailor SWAT watershed
854 delineations to lake and reservoir waterbodies, *Environ. Model. Softw.*, 108, 67–71,
855 <https://doi.org/10.1016/j.envsoft.2018.07.003>, 2018.
856
857 Moriasi, D. N., Gitau, M. W., Pai, N., and Daggupati, P.: Hydrologic and water quality models:
858 Performance measures and evaluation criteria, *Trans. ASABE*, 58, 1763–1785,
859 <https://doi.org/10.13031/trans.58.10715>, 2015.
860
861 Muche, M. E., Sinnathamby, S., Parmar, R., Knightes, C. D., Johnston, J. M., Wolfe, K., Purucker,



- 862 S. T., Cyterski, M. J., and Smith, D.: Comparison and Evaluation of Gridded Precipitation
863 Datasets in a Kansas Agricultural Watershed Using SWAT, *JAWRA J. Am. Water Resour.*
864 *Assoc.*, 56, 486–506, <https://doi.org/10.1111/1752-1688.12819>, 2020.
- 865
866 Mukhopadhyay, S., Sankarasubramanian, A., and de Queiroz, A. R.: Performance Comparison
867 of Equivalent Reservoir and Multireservoir Models in Forecasting Hydropower Potential for
868 Linking Water and Power Systems, *J. Water Resour. Plan. Manag.*, 147, 04021005,
869 [https://doi.org/10.1061/\(ASCE\)WR.1943-5452.0001343](https://doi.org/10.1061/(ASCE)WR.1943-5452.0001343), 2021.
- 870
871 Nash, J. E. and Sutcliffe, J. V.: River flow forecasting through conceptual models part I — A
872 discussion of principles, *J. Hydrol.*, 10, 282–290, [https://doi.org/10.1016/0022-1694\(70\)90255-6](https://doi.org/10.1016/0022-1694(70)90255-6),
873 1970.
- 874
875 Nathan, R. and Lowe, L.: The Hydrologic Impacts of Farm Dams, *Australas. J. Water Resour.*, 16,
876 75–83, <https://doi.org/10.7158/13241583.2012.11465405>, 2012.
- 877 Census of agriculture: <https://www.nass.usda.gov/AgCensus/index.php>, last access: 10
878 February 2021.
- 879
880 Ni, X. and Parajuli, P. B.: Evaluation of the impacts of BMPs and tailwater recovery system on
881 surface and groundwater using satellite imagery and SWAT reservoir function, *Agric. Water*
882 *Manag.*, 210, 78–87, <https://doi.org/10.1016/j.agwat.2018.07.027>, 2018.
- 883
884 Ni, X., Parajuli, P. B., and Ouyang, Y.: Assessing Agriculture Conservation Practice Impacts on
885 Groundwater Levels at Watershed Scale, *Water Resour. Manag.*, 34, 1553–1566,
886 <https://doi.org/10.1007/s11269-020-02526-3>, 2020.
- 887
888 Ogilvie, A., Belaud, G., Massuel, S., Mulligan, M., Le Goulven, P., Malaterre, P.-O., and Calvez, R.:
889 Combining Landsat observations with hydrological modelling for improved surface water
890 monitoring of small lakes, *J. Hydrol.*, 566, 109–121, <https://doi.org/10.1016/j.jhydrol.2018.08.076>,
891 2018.
- 892
893 Ogilvie, A., Poussin, J.-C., Bader, J.-C., Bayo, F., Bodian, A., Dacosta, H., Dia, D., Diop, L., Martin,
894 D., and Sambou, S.: Combining Multi-Sensor Satellite Imagery to Improve Long-Term
895 Monitoring of Temporary Surface Water Bodies in the Senegal River Floodplain, *Remote*
896 *Sens.*, 12, 3157, <https://doi.org/10.3390/rs12193157>, 2020.
- 897
898 Perin, V., Roy, S., Kington, J., Harris, T., Tulbure, M. G., Stone, N., Barsballe, T., Reba, M., and
899 Yaeger, M. A.: Monitoring Small Water Bodies Using High Spatial and Temporal Resolution
900 Analysis Ready Datasets, *Remote Sens.*, 13, 5176, <https://doi.org/10.3390/rs13245176>, 2021a.
- 901
902 Perin, V., Tulbure, M. G., Gaines, M. D., Reba, M. L., and Yaeger, M. A.: On-farm reservoir
903 monitoring using Landsat inundation datasets, *Agric. Water Manag.*, 246, 106694,
904 <https://doi.org/10.1016/j.agwat.2020.106694>, 2021b.
- 905
906 Perin, V., Tulbure, M. G., Gaines, M. D., Reba, M. L., and Yaeger, M. A.: A multi-sensor satellite
907 imagery approach to monitor on-farm reservoirs, *Remote Sens. Environ.*,
908 <https://doi.org/10.1016/j.rse.2021.112796>, 2022.
- 909
910 Perrin, J.: Assessing water availability in a semi-arid watershed of southern India using a semi-
911 distributed model, *J. Hydrol.*, 13, 2012.
- 912
913 Pinhati, F. S. C., Rodrigues, L. N., and Aires de Souza, S.: Modelling the impact of on-farm
914 reservoirs on dry season water availability in an agricultural catchment area of the Brazilian



- 915 savannah, *Agric. Water Manag.*, 241, 106296, <https://doi.org/10.1016/j.agwat.2020.106296>, 2020.
916
917 PRISM Gridded Climate Data: <https://prism.oregonstate.edu/>, last access: 2 January 2022.
918 Rabelo, U. P., Dietrich, J., Costa, A. C., Simshäuser, M. N., Scholz, F. E., Nguyen, V. T., and Lima
919 Neto, I. E.: Representing a dense network of ponds and reservoirs in a semi-distributed
920 dryland catchment model, *J. Hydrol.*, 603, 127103, <https://doi.org/10.1016/j.jhydrol.2021.127103>,
921 2021.
922
923 Renwick, W. H., Smith, S. V., Bartley, J. D., and Buddemeier, R. W.: The role of impoundments
924 in the sediment budget of the conterminous United States, *Geomorphology*, 71, 99–111,
925 <https://doi.org/10.1016/j.geomorph.2004.01.010>, 2005.
926
927 Rodrigues, L. N., Sano, E. E., Steenhuis, T. S., and Passo, D. P.: Estimation of Small Reservoir
928 Storage Capacities with Remote Sensing in the Brazilian Savannah Region, *Water Resour.*
929 *Manag.*, 26, 873–882, <https://doi.org/10.1007/s11269-011-9941-8>, 2012.
930
931 Sawunyama, T., Senzanje, A., and Mhizha, A.: Estimation of small reservoir storage capacities
932 in Limpopo River Basin using geographical information systems (GIS) and remotely sensed
933 surface areas: Case of Mzingwane catchment, *Phys. Chem. Earth Parts ABC*, 31, 935–943,
934 <https://doi.org/10.1016/j.pce.2006.08.008>, 2006.
935
936 Schreider, S. Yu., Jakeman, A. J., Letcher, R. A., Nathan, R. J., Neal, B. P., and Beavis, S. G.:
937 Detecting changes in streamflow response to changes in non-climatic catchment conditions:
938 farm dam development in the Murray–Darling basin, Australia, *J. Hydrol.*, 262, 84–98,
939 [https://doi.org/10.1016/S0022-1694\(02\)00023-9](https://doi.org/10.1016/S0022-1694(02)00023-9), 2002.
940
941 Soil Survey Staff, USDA-NRCS: Gridded Soil Survey Geographic (gSSURGO) Database for the
942 Conterminous United States. United States Department of Agriculture, Natural Resources
943 Conservation Service., 2021.
944
945 Publications | Soil & Water Assessment Tool (SWAT): <https://swat.tamu.edu/publications/>, last
946 access: 17 June 2022.
947
948 Tapley, B. D., Bettadpur, S., Watkins, M., and Reigber, C.: The gravity recovery and climate
949 experiment: Mission overview and early results, *Geophys. Res. Lett.*, 31, n/a–n/a,
950 <https://doi.org/10.1029/2004GL019920>, 2004.
951
952 Thompson, J. C.: Impact and Management of Small Farm Dams in Hawke's Bay, New Zealand,
953 thesis, Open Access Te Herenga Waka-Victoria University of Wellington,
954 <https://doi.org/10.26686/wgtn.16997929.v1>, 2012.
955
956 United States Geological Survey Water Data for the Nation: <https://waterdata.usgs.gov/nwis>,
957 last access: 22 June 2022.
958
959 Van Den Hoek, J., Getirana, A., Jung, H., Okeowo, M., and Lee, H.: Monitoring Reservoir
960 Drought Dynamics with Landsat and Radar/Lidar Altimetry Time Series in Persistently Cloudy
961 Eastern Brazil, *Remote Sens.*, 11, 827, <https://doi.org/10.3390/rs11070827>, 2019.
962
963 Van Der Zaag, P. and Gupta, J.: Scale issues in the governance of water storage projects,
964 *Water Resour. Res.*, 44, <https://doi.org/10.1029/2007WR006364>, 2008.
965
966 Vanthof, V. and Kelly, R.: Water storage estimation in ungauged small reservoirs with the
967 TanDEM-X DEM and multi-source satellite observations, *Remote Sens. Environ.*, 235, 111437,



- 968 <https://doi.org/10.1016/j.rse.2019.111437>, 2019.
969
970 Verpoorter, C., Kutser, T., Seekell, D. A., and Tranvik, L. J.: A global inventory of lakes based on
971 high-resolution satellite imagery, *Geophys. Res. Lett.*, 41, 6396–6402,
972 <https://doi.org/10.1002/2014GL060641>, 2014.
973
974 Vörösmarty, C. J., McIntyre, P. B., Gessner, M. O., Dudgeon, D., Prusevich, A., Green, P., Glidden,
975 S., Bunn, S. E., Sullivan, C. A., Liermann, C. R., and Davies, P. M.: Global threats to human water
976 security and river biodiversity, *Nature*, 467, 555–561, <https://doi.org/10.1038/nature09440>, 2010.
977
978 Yaeger, M. A., Reba, M. L., Massey, J. H., and Adviento-Borbe, M. A. A.: On-farm irrigation
979 reservoirs in two Arkansas critical groundwater regions: A comparative inventory, *Appl. Eng.*
980 *Agric.*, 33, 869–878, <https://doi.org/10.13031/aea.12352>, 2017.
981
982 Yaeger, M. A., Massey, J. H., Reba, M. L., and Adviento-Borbe, M. A. A.: Trends in the
983 construction of on-farm irrigation reservoirs in response to aquifer decline in eastern
984
985 Arkansas: Implications for conjunctive water resource management, *Agric. Water Manag.*,
986 208, 373–383, <https://doi.org/10.1016/j.agwat.2018.06.040>, 2018.
987
988 Yao, F., Wang, J., Yang, K., Wang, C., Walter, B. A., and Crétaux, J. F.: Lake storage variation on
989 the endorheic Tibetan Plateau and its attribution to climate change since the new
990 millennium, *Environ. Res. Lett.*, 13, <https://doi.org/10.1088/1748-9326/aab5d3>, 2018.
991
992 Yapo, P. O., Gupta, H. V., and Sorooshian, S.: Automatic calibration of conceptual rainfall-runoff
993 models: sensitivity to calibration data, *J. Hydrol.*, 181, 23–48, [https://doi.org/10.1016/0022-](https://doi.org/10.1016/0022-1694(95)02918-4)
994 [1694\(95\)02918-4](https://doi.org/10.1016/0022-1694(95)02918-4), 1996.
995
996 Yongbo, L., Wanhong, Y., Zhiqiang, Y., Ivana, L., Jim, Y., Jane, E., and Kevin, T.: Assessing Effects
997 of Small Dams on Stream Flow and Water Quality in an Agricultural Watershed, *J. Hydrol.*
998 *Eng.*, 19, 05014015, [https://doi.org/10.1061/\(ASCE\)HE.1943-5584.0001005](https://doi.org/10.1061/(ASCE)HE.1943-5584.0001005), 2014.
999
1000 Zhang, C., Peng, Y., Chu, J., Shoemaker, C. A., and Zhang, A.: Integrated hydrological modelling
1001 of small- and medium-sized water storages with application to the upper Fengman Reservoir
1002 Basin of China, *Hydrol Earth Syst Sci*, 15, <https://doi.org/10.5194/hess-16-4033-2012>, 2012.
1003
1004 Zhang, S., Foerster, S., Medeiros, P., de Araújo, J. C., Motagh, M., and Waske, B.: Bathymetric
1005 survey of water reservoirs in north-eastern Brazil based on TanDEM-X satellite data, *Sci. Total*
1006 *Environ.*, 571, 575–593, <https://doi.org/10.1016/j.scitotenv.2016.07.024>, 2016.
1007
1008
1009